Supplementary Information

Photopatterned oil-reservoir micromodels with tailored wetting properties

Hyundo Lee, Seung Goo Lee and Patrick S. Doyle *

I. Comparison of micromodel fabrication, wettability tailoring methods

		Wettability range	Wettability tailoring method	Micromodel material	Wettability modification process time	Micromodel fabrication method
Heterogeneous (spatially patterned wettability in a microchannel)	Schneider et al.[1]	**Binary** : water-wet (θ=180°) and oil-wet (θ=30°) (θ: hexadecane in water)	UV-initiated, poly(acrylic acid) graft patterning	PDMS	> 4 hours	Soft lithography
	Ma et al.[2]	**Binary** : hydrophilic (θ=7.5°) and hydrophobic (θ=96°) (θ: water in air)	UV-ozone, surface oxidize patterning	PDMS	> 2 days	Soft lithography
	Levaché et al.[3]	**Continuous range** : water-wet (θ=35°) and oil-wet (θ=110°) (θ: water in hexadecane)	Deep UV exposure patterning	NOA81 (thiolene-based UV-curable resin)	< 1 hour	Soft lithography
	Murison et al.[4]	**Binary** : water-wet and oil-wet (characterized by capillary-pressure saturation)	Gold and chlorotrimethoxysilane coatings on glass beads	Glass beads	> 19 hours	Functionalized glass beads packing
	Copolymerization method	**Continuous range** : water-wet (θ=60°) and oil-wet (θ=144°) (θ: water in decane)	UV-initiated copolymerization	Glass (wall) and polymer (microstructures)	< 1 hour	Photolithography
Homogeneous (the entire surface of a microchannel has the same wettability)	Gunda et al.[5]	Hydrophilic (silicon and glass)	–	Silicon and glass	–	Inductively coupled plasma reactive ion etching
	Wu et al.[6]	Water-wet (within 1 hour of bonding), oil-wet (after 24 hours of bonding)	Oxygen plasma	PDMS and glass	–	Soft lithography
	de Haas et al.[7]	Water-wet (glass)	–	Glass	–	Hydrofluoric acid, nitric acid etching
	Grate et al.[8]	Oil-wet (θ=140°) (θ: water in hexadecane)	Silanization	Silicon and glass	–	Inductively coupled plasma reactive ion etching
	Song et al.[9]	Hydrophilic (calcite and glass)	–	Calcite and glass	–	Hydrochloric acid etching

II. Contact angle measurement setup and procedure

There are ongoing debates on proper droplet sizes and procedures in sessile drop contact angle measurements [10-16]. If the size of the droplet is too big, sagging or flattening of the droplet due to the gravity deforms the profile of the droplet from a spherical shape. This gravity-induced sagging eventually amplifies contact angle values and leads to overestimated values for large contact angles [13,14,17]. For the case of small contact angles, when the volume of the droplet is too small, the receding contact angles may not reach their receding contact angles before the droplet is removed [12,15]. Thus, measurements of advancing and receding contact angles are more difficult in the high and low contact angle regimes (near 0, 180°).

Therefore, contact angles have to be measured carefully at the consistent measurement process. In this study, the polymeric substrates were prepared with precursor solutions of tabulated concentrations, cured under the UV lamp (wavelength 365 nm) for 3 minutes, and thoroughly rinsed with acetone to remove any uncured precursor (Fig. S1–B). A quartz container filled with decane (Sigma-Aldrich) was located on the measurement stage of the contact angle goniometer (Ramé -Hart). The prepared substrate was immersed in the decane-filled quartz container, and the needle was set on the above of the substrate surface. Water was infused and withdrawn at a constant injecting/retracting rate (5 ml/hr) by a syringe pump (Harvard Apparatus), and the maximum volume of the droplet was 20 µl. The advancing and receding contact angles were measured with an image software (DROPimage Advanced, Ramé-Hart) when there was an evident contact line change, advanced or retreated, approximately 1 minute after infusion or withdrawal of water was stopped. All measurements were repeated three times and the average contact angles and the standard deviations were plotted in the graph (Fig. 2).

During the advancing contact angle measurement, to minimize the disturbance of needle tip removal, the measurement was conducted following the protocol proposed by Drelich [16]. After depositing the first small drop onto the substrate, the needle tip was detached from the drop and lifted a few millimeters above the deposited drop and centered at the droplet. Additional water was supplied and fused into the deposited drop, and enlarged (Fig. S1–C). To measure the receding angle, the needle tip attached to the droplet again, and the syringe pump retracted the water at the same rate of infusion. When the decrease in the droplet base diameter was observed, the syringe pump was stopped, the needle was slowly removed from the droplet, and the receding contact angle was measured with the software after 1 minute for stabilization [12,15,16] (Fig. S1–D).

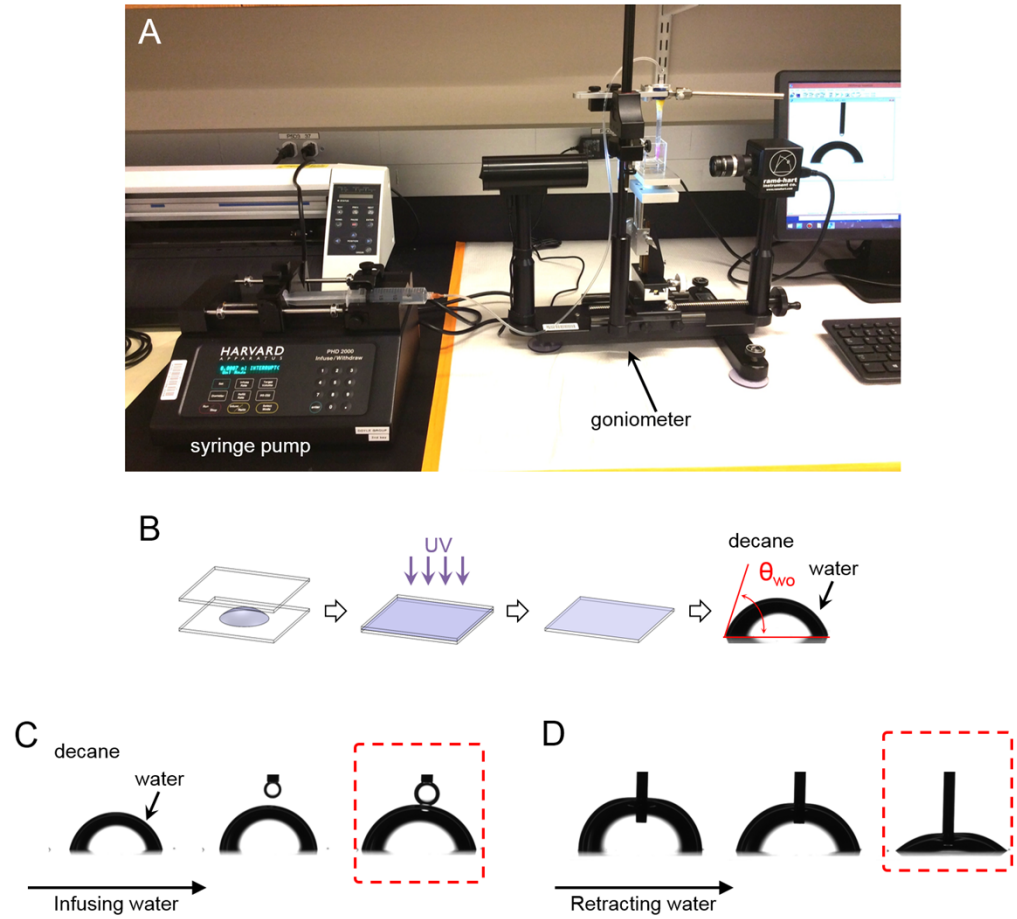

Fig. S1 – (A) Contact angle measurement setup with a syringe pump (Harvard Apparatus) and a goniometer (Ramé-Hart). (B) Substrates were prepared by pressing a drop of the precursor solution on an acrylated glass. (C) Advancing contact angles were measured when the droplet showed constant contact angle while the volume and the diameter of the droplet is increasing. (D) Receding contact angles were measured when the movement of the contact line was detected. Infusing/retracting rates were 5 ml/hr, and the maximum volume of the droplet was 20 µl.

III. Sequential images of the fluid displacement process

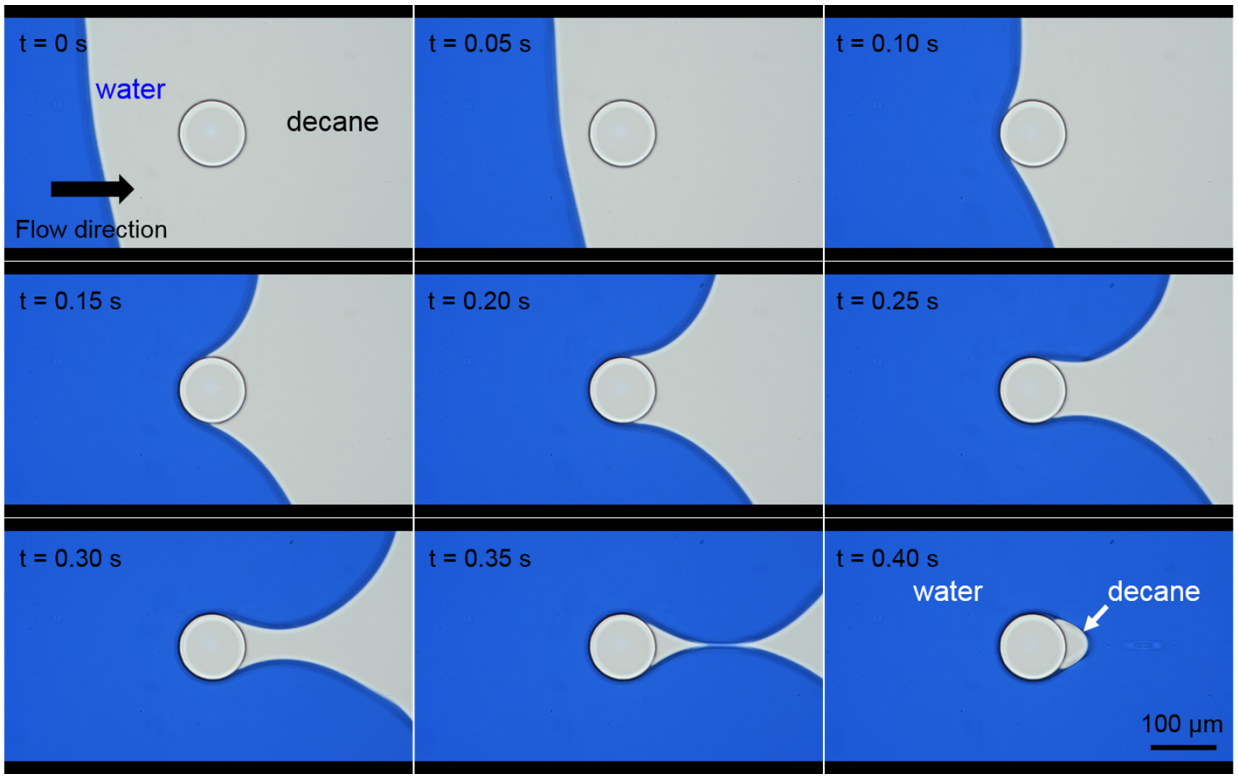

Fig. S2 – Sequential images were taken for an immiscible fluids displacement experiment with an oleophilic post (O-1, HDDA 15%, LA 80%, Darocur 1173 5%). Single oleophilic posts were made in a microfluidic channel. After rinsing the channel with acetone to remove uncured precursor solution, the channel was first filled with decane, and water was introduced to displace decane. The time-lapse video showing this process is also available in the accompanying electronic supplementary information (ESI†).

IV. Single post, immiscible fluid displacement validation with OpenFOAM 2.3.0

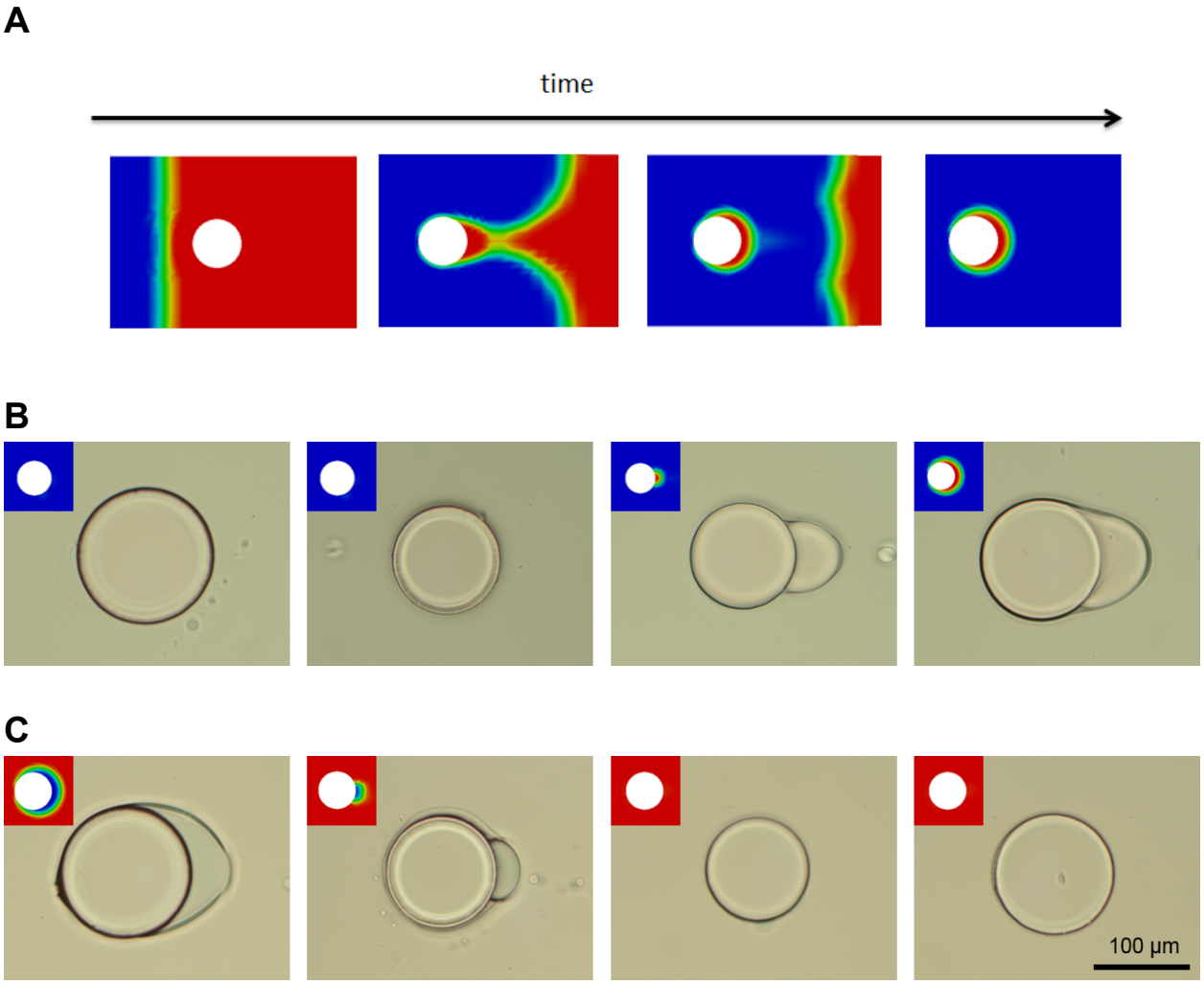

Fig. S3 – Computational simulation for the immiscible fluid displacement with OpenFOAM 2.3.0, Volume of Fluid (VOF) method. In VOF method, we solve the continuity equations for both phases based on "volume fraction". Volume fraction is the probability of the phase to be present in that region. We also solve the momentum conservation equation that helps us include the surface tension forces between the phases. (A) Sequential images of decane displacement by water for the oleophilic post (O–1). In this figure, red and blue indicate decane and water phase respectively. (B), (C) Validation of displacement flow experiments presented in Fig. 4 with computational simulation. Simulation results are shown as inset images.

The Volume of Fluid (VOF) method was used to model the flow. The model uses α, the volume fraction of dispersed phase as an additional variable in addition to $\rho, \mu, \vec{u}, P$ (density, viscosity, velocity, and pressure).

VOF methods are as follows:

$$\rho\left(\frac{\partial\vec{u}}{\partial t}+(\vec{u}.\nabla)\vec{u}\right)=-\nabla P+\nabla.(\mu S)+f \tag{1}$$

$$\nabla.\vec{u}=0 \tag{2}$$

$$\frac{\partial\alpha}{\partial t}+\vec{u}.\nabla\alpha=0 \tag{3}$$

$$\rho=\rho_1(1-\alpha)+\rho_2\alpha \tag{4}$$

$$\mu=\mu_1(1-\alpha)+\mu_2\alpha \tag{5}$$

$$f=\sigma k\frac{2\rho}{\rho_1+\rho_2}\nabla\alpha \tag{6}$$

$$k=-\nabla.\hat{n} \tag{7}$$

$$\hat{n}=\frac{\nabla\alpha}{|\nabla\alpha|} \tag{8}$$

$$S_{ij}=\frac{1}{2}\left(\frac{\partial u_j}{\partial x_i}+\frac{\partial u_i}{\partial x_j}\right) \tag{9}$$

Equation (1) and Equation (2) are classical momentum conservation and continuity equations. However, in Equation (1), we also have a variable f which is surface tension coupling between the two phases. f has been defined in Equation (6). In Equation (6), k is known as curvature which in turns depends on a interface normal defined from volume fraction (as done in Equation (7) and Equation (8)). Equation (3) is for mass balance around a phase. The overall density and viscosity used in Equation (1) are calculated from Equation (4) and Equation (5). If we want to include the effect of contact angle with the solid walls, we modify the usually calculate normal from Equation (8) by breaking it into normal and tangential components with respect to wall and multiplying with contact angle components. Mathematically this is done as follows:

$$\hat{n}=\hat{n_w}\cos\theta+\hat{t_w}\sin\theta \tag{10}$$

We used OpenFOAM to create the geometry with velocity inlet boundary conditions and pressure outlet boundary conditions. All other surfaces were made stationary walls where we could specify contact angles.

V. Swelling ratio measurements

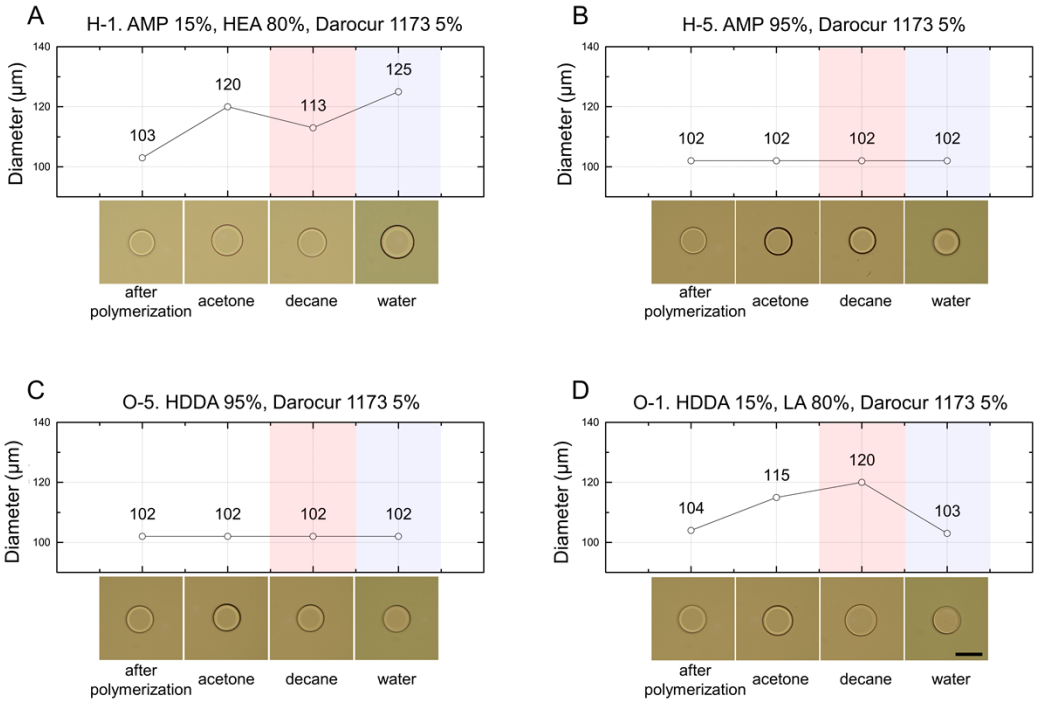

Fig. S4 – The diameters of single posts with different chemical compositions were investigated after polymerization, in acetone, in decane, and in water. Since the diameter of a circle in the photomask used for UV lithography was 790 μm, the diameters of posts have to be 101 μm with a 20x microscope objective lens (projection factor = 7.8). Right after polymerization, all 4 posts showed the same diameters, approximately 103 μm. (A) The most hydrophilic post, H-1, was swelled, and its diameter was increased around 25% in water (B, C) The intermediate posts, H-5 and O-5, without hydrophilic and oleophilic monomers maintained their sizes in different solutions. (D) The most oleophilic post, O-1, was swelled in decane, and its diameter was increased around 20%. Scale bar is 100 μm. (AMP: 1-(acryloyloxy)-3-(methacryloyloxy)-2-propanol, HEA: 2-hydroxyethyl acrylate, HDDA: 1,6-hexanediol diacrylate, LA: lauryl acrylate)

VI. Verification of reproducibility of fabrication method and flow experiment

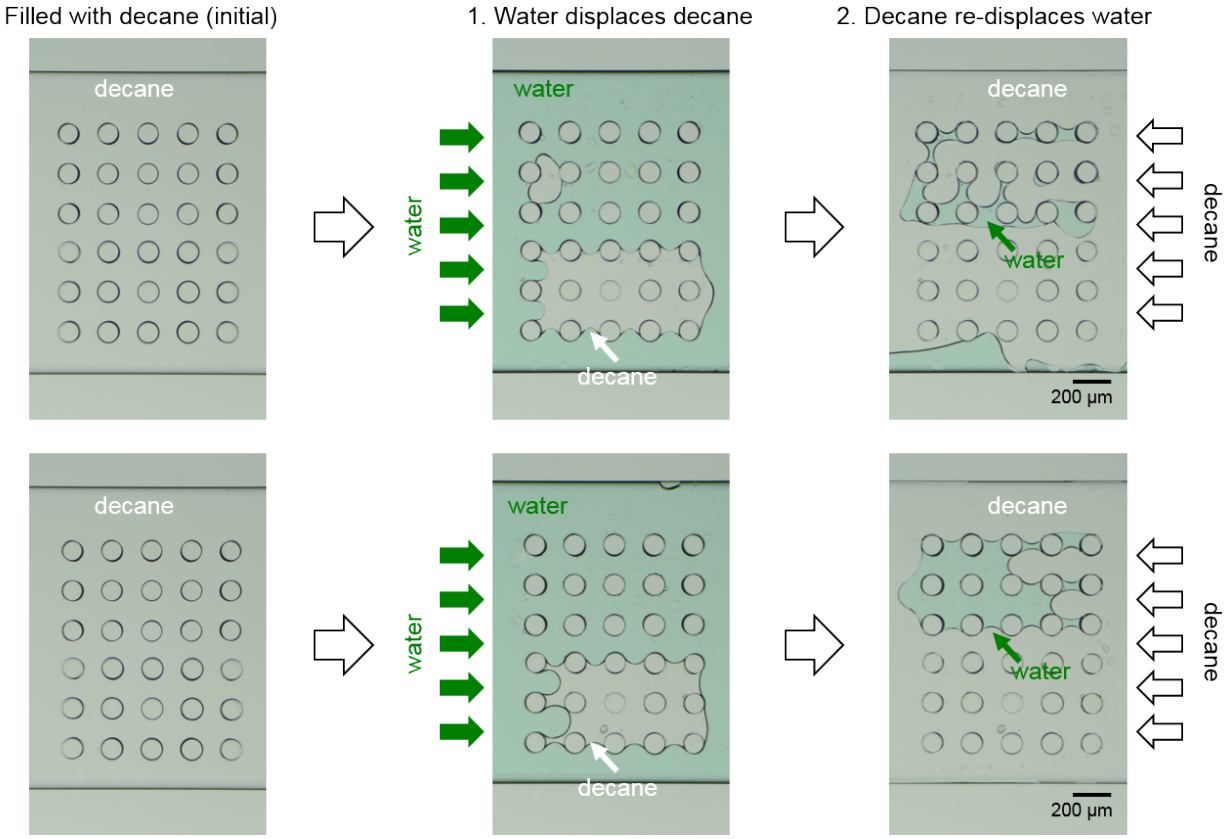

Fig. S5 – We reproduced two microfluidic models having the same multi-post configuration as Fig. 6 to demonstrate the robustness of the fabrication procedure. We also reproduced the same immiscible flow experiment to address the reproducibility of flow experiment with each device.

References

1. M. H. Schneider; and P. Tabeling, Am. J. Appl. Sci., 2011, 8, 927–932.
2. K. Ma, J. Rivera, G. J. Hirasaki, and S. L. Biswal, J. Colloid Interface Sci., 2011, 363, 371–378.
3. B. Levaché, A. Azioune, M. Bourrel, V. Studer, and D. Bartolo, Lab Chip, 2012, 12, 3028–3031.
4. J. Murison, B. Semin, J.-C. Baret, S. Herminghaus, M. Schröter, and M. Brinkmann, Phys. Rev. Appl., 2014, 2, 034002.
5. N. S. K. Gunda, B. Bera, N. K. Karadimitriou, S. K. Mitra, and S. M. Hassanizadeh, Lab Chip, 2011, 11, 3785–3792.
6. M. Wu, F. Xiao, R. M. Johnson-Paben, S. T. Retterer, X. Yin, and K. B. Neeves, Lab Chip, 2012, 12, 253–261.
7. T. W. de Haas, H. Fadaei, U. Guerrero, and D. Sinton, Lab Chip, 2013, 13, 3832–3839.
8. J. W. Grate, M. G. Warner, J. W. Pittman, K. J. Dehoff, T. W. Wietsma, C. Zhang, and M. Oostrom, Water Resour. Res., 2013, 49, 4724–4729.
9. W. Song, T. W. de Haas, H. Fadaei, and D. Sinton, Lab Chip, 2014, 14, 4382–4390.
10. R. J. Good and M. N. Koo, J. Colloid Interface Sci., 1979, 71, 283–292.
11. A. Marmur, J. Colloid Interface Sci., 1994, 168, 40–46.
12. C. Lam, R. Wu, D. Li, M. Hair, and a Neumann, Adv. Colloid Interface Sci., 2002, 96, 169–191.
13. C. W. Extrand and S. I. Moon, Langmuir, 2010, 26, 11815–22.
14. S. Srinivasan, G. H. McKinley, and R. E. Cohen, Langmuir, 2011, 27, 13582-13589.
15. J. T. Korhonen, T. Huhtama, O. Ikkala, and R. H. A. Ras, Langmuir, 2013, 29, 3858-3863.
16. J. Drelich, Surf. Innov., 2013, 1–7.
17. D. Quéré and M. Reyssat, Philos. Trans. A. Math. Phys. Eng. Sci., 2008, 366, 1539–56.